A coupling approach between metallic bipolar plates corrosion and membrane chemical degradation in the proton exchange membrane fuel cells

I. Elferjani, G. Serre, B. Ter-Ovanessian, B. Normand

Version of Record: https://www.sciencedirect.com/science/article/pii/S0360319921025039
Manuscript_e7ea10b3a3e0b741fb851178f06a3b7c

A coupling approach between metallic bipolar plates corrosion and membrane chemical degradation in the Proton Exchange Membrane Fuel Cells

I.ELFERJANI[a,b], G.SERRE[b], B.TER-OVANESSIAN[a], B.NORMAND[a]

[a]*Université de Lyon, INSA-LYON, MATEIS UMR CNRS 5510, 69621 Villeurbanne, France*

[b]*CEA, LITEN, DEHT, F-38054, Grenoble, France*

ARTICLE INFO

Article history:
Received
Received in revised form
Accepted

Keywords:
Proton exchange membrane fuel cell
Bipolar plates 'Corrosion
Ionic transport
Fenton mechanism
Membrane degradation modelling
Coupling model
NEDC cycles

ABSTRACT

The Nafion membrane's chemical degradation by the Fenton mechanism involves the presence of ferrous ions Fe^{2+} but the detrimental concentration is not well known. These ions could be generated either from the balance of plant or from the bipolar plates' corrosion. As an attempt to describe the link between the two mechanisms, the membrane's degradation and the bipolar plates' corrosion were investigated. Our work is based on experimental and modelling approaches. We start with a parametric corrosion study allowing the determination of the Fe^{2+} flux using a Look-Up Table. The second step is the modelling of the Fe^{2+} effect on the membrane degradation. The third is the modelling of ionic species transport between the bipolar plates and the membrane. The final coupled degradation model is implemented in a PEMFC performance simulator based on the Matlab/Simulink® platform. The model is used to simulate the degradation mechanism during NEDC (New European Driving Cycle).

GRAPHICAL ABSTRACT

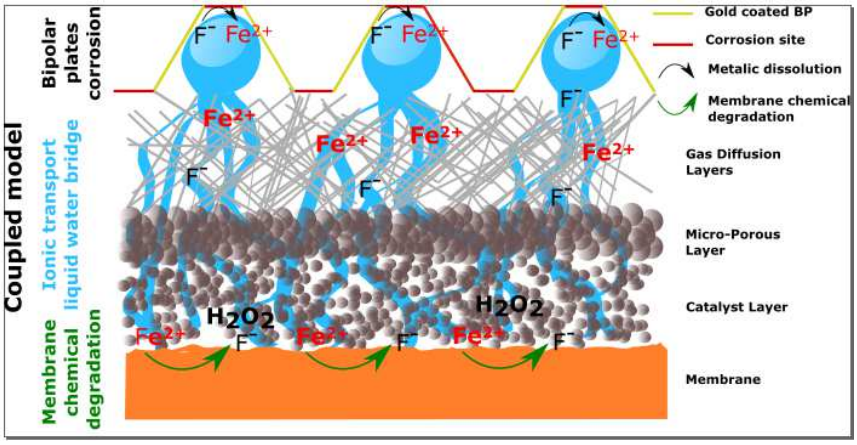

Introduction

The transportation sector represents a major source of greenhouse gas emissions, about one third of the total emissions in the last five years ([1]-[2]-[3]). The development and the commercialization of fuel cells electric vehicles is one of the promising alternatives in the path of decarbonizing the transport sector. Low temperature proton exchange membrane fuel cells (PEMFC) are one of the most frequently used types of fuel cells in the automotive sector [4].

Even if the PEMFC technology made the core of large research, the wide market implementation is not yet reached. The main challenges facing this technology are the high cost of production and the limited durability of components such as the bipolar plates (BP), the catalyst layer and the membrane, hence a limited long-term reliability of the cells [5] [6]. The degradation mechanisms attacking PEMFC are either reversible or irreversible. The BPs' corrosion, the membrane degradation, the GDL's degradation and the catalyst dissolution represent some of the irreversible ones [7] [8] [9]. In the case of BPs 'corrosion, some solution requiring performant coating development have been investigated [10] [11] [12]. However, whatever the solution, the prediction of degradation behavior is essential. It allows a better knowledge of the system's requirements in terms of materials, designs and optimal working conditions. Usually, two approaches are available. The first is the experimental testing with either *in-situ* and *ex-situ* ageing or Accelerated Stress Tests (AST) while the second approach is based on modelling [13] [14]. Each approach has its benefits and drawbacks. Ageing-testing in real conditions, implies a long-term results feedback (thousands of hours). The AST are often criticized for the lack of precision and the non-representativity of the normal operating conditions.

Conversely, simulation based on experimentally validated models can enhance the development and the control of a PEMFC system, by predicting the cell's life time for various components and various working conditions ([15]-[16]).
In the present paper, the metallic BPs' corrosion, the polyfluorinated sulfonic acid membrane's chemical degradation and the synergic effects in between the two phenomena were investigated in-depth. To our knowledge, bipolar plates' corrosion in the fuel cell was mainly studied experimentally and not widely modelled in a PEMFC performance code ([17]-[18]-[19]). While the membrane degradation has been explored and modelled in many codes ([20]-[21]-[22]-[23]). An excellent discussion of various degradation phenomena can be found in the reviews by Tawfik *et al.* [18] and Wang *et al.* [24] as well as Janhkle *et al.*[25]. Many mechanisms and their corresponding kinetics have been then reported. Based on that, several chemical degradation models have been presented ([26]-[27]-[28]).
However, only few developed models which describe the PEMFC performances and predict ageing, focus on coupled degradation phenomena with considering the complex interactions among the components. The membrane's chemical degradation induced by the ferrous ions released from the BPs' corrosion is an example of this complex interaction. On one side, the effect of the variation of the ferrous ions concentration on the membrane degradation has been studied. It is assumed to catalyze the Fenton mechanism, but with a lack of data relative to its real concentration under operating conditions. On the other side, the bipolar plates' corrosion is enhanced by the fluorides emitted from the membrane's degradation. Thus, it appears that the degradation of bipolar plates and membrane are interdependent through the release of ionic species such as ferrous ions Fe^{2+} [29] and fluoride ions F^-. The present paper focuses on this synergic degradation through a coupling approach in a PEMFC performance model on Matlab/Simulink® software. For this problematic, a comprehensive global PEMFC system model is required. We use a multiphysical code called MePHYSTO-FC (Multiphysical Simulation Tool for Fuel Cell) developed on Matlab/Simulink® at CEA Grenoble. This code is integrated in the global numerical platform MUSES that includes several calculation codes at multiples spatial scales and for different generators and electrochemical energy converters such as fuel cells, electrolyzers and also batteries. MePHYSTO-FC is a 2D/1D model. It simulates the performance of the fuel cell and its possible degradations. In the last 20 years, this code has been developed and endowed to include new parameters and to consider new degradations mechanisms. It was used by many collaborators and industrials to address specific needs and problematics related to the PEMFC ([30]-[31]-[32]-[33]) . Further information regarding the MePHYSTO's structure and the equations used in the code are detailed in the Appendix section.

1 Methods and approaches used

To understand the impact of the BPs' corrosion on the membrane's chemical degradation and its influence on the cell's lifetime, we adopted a specific approach illustrated in the Fig. 1. The three main topics treated in this paper: bipolar plates' corrosion, membrane chemical degradation and ionic species transport are covered from different angles.
The corrosion of 316L SS plates was studied with potentiodynamic measurements in order to collect experimental data. While the membrane's chemical degradation was modeled and later validated with different *ex-situ* tests. Then, the ionic species transport was modeled. These three bricks were first treated independently before the models' coupling. Therefore, each brick was discussed in a specific section.
Consequently, this paper is organized as follows: the introduction and section 1 introduce the scope of the work and the method used for the analysis and the model's development. The section 2 is the corrosion study, it provides the iron ions emission term. The results of this experimental study are stored in a Look Up Table (LUT). The created LUT is connected to the channels in the code where the local conditions requested as inputs for this LUT, are calculated. The section 3 consists in modelling the membrane's chemical degradation that provides the fluoride emission. The section 4 is the modelling of the ionic species transport between the membrane and the BPs through the GDE (Gas Diffusion Layer/Microporous layer/ Catalyst Layer). It is developed in order to connect the two degradation mechanisms. Finally, the code is used to simulate a New European Driving Cycle (NEDC) in order to follow the evolution of fluoride and ferrous ions' concentrations over time.

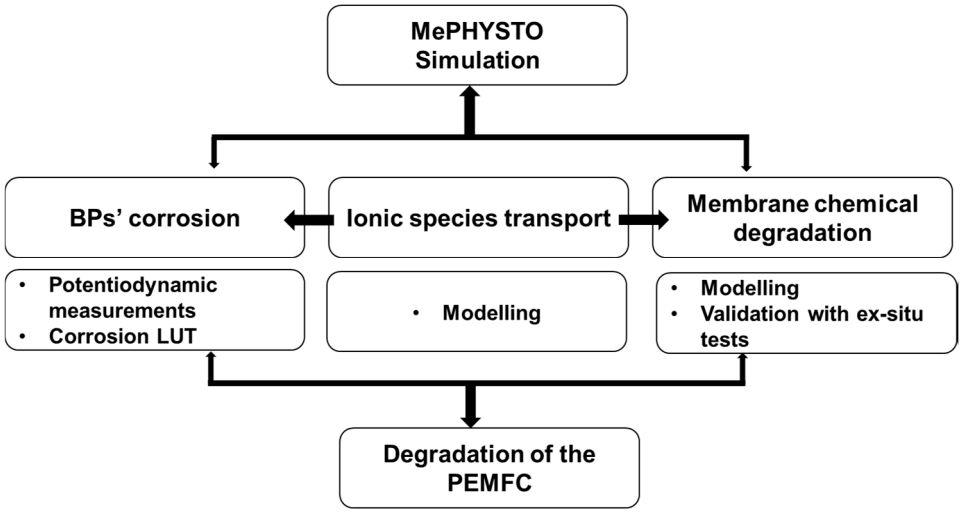

Fig. 1-The Approach's structure.

2 Corrosion study

2.1. Stainless steel 316L corrosion

Bipolar plates made up of stainless steel (SS) substrate and protected with performant coatings, are often represented as a good compromise between the cost and functional properties, because of their good electrical and thermal conductivities [18] [8], easy formability

and low cost [34]. In this context, a commercial 316L stainless steel is chosen as a reference material for the parametric corrosion study. The 316L SS is known for its corrosion resistance properties relative to its passive layer. The nominal specimen composition provided by the supplier is 0.03 C, 0.001 S, 0.021 P, 0.44 Si, 1.84 Mn, 2.47 Mo, 12.3 Ni, 17.54 Cr, balance Fe in weight%.

2.2. Corrosion parametric study

For the corrosion study, potentiodynamic measurements were carried out on a thermally controlled three electrodes cell. The three electrodes are: 316L stainless steel sample as working electrode, a saturated mercury sulphate as reference electrode (V_{MSE}=658mV vs SHE) and the counter electrode is graphite rod. The stainless steel plates were cleaned with acetone solution then dried and cut to 1 cm^2 of 0.3 mm thickness samples. The three electrodes are connected with a Gamry ref 600 potentiostat. The electrochemical sequence starts with 12 hours Open Circuit Potential (OCP) followed by a potentiodynamic measurement performed at a scanning rate of 0.5 mV/s. The polarization curve gives the variations of the current density as a function of the potential. In order to simulate the PEMFC working environment, the measurements were carried out at temperatures 333 K, 343 K and 353 K. The temperature control and variation, were insured through a heated water circulation connected to a heating bath. The cells were continuously bubbled with air. The different electrolytes were prepared with 18 MΩ ultrapure water at different chloride contents 10^{-2} M, 10^{-3} M and 10^{-4} M. Chlorides are here substituted for fluorides released by membrane degradation for laboratory security restrictions. As halides chloride and fluoride ions allow similar damages, especially in the cases of localized corrosion of stainless steel. Different pH values are considered (3.5, 4, 4.5 and 5).

The Fig. 2 shows an example of variation of the potentiodynamic curves as a function of chloride concentration, at fixed temperature and pH (T=353 K, pH=3.5). The anodic part of the potentiodynamic curves for chloride concentrations 10^{-2} M and 5.10^{-3} M have relatively similar patterns but still different from the rest of the curves for lower concentrations. Passive steels such as 316L, are generally characterised by a passive behaviour with low current density at wide potential range (blue and green curves). However, the exposure of 316L SS to high concentrations of chloride ions (black and red curves), causes pitting corrosion and the current density quickly reaches important values. Indeed, the defects present in the passive film allow the possible incorporation of the chlorides present in abundance on the surface which contributes to the initiation of the pitting. Once one or more pits have been initiated, the material is intensively dissolved. This stage induces on the potentiodynamic curve, an increase of the current density indicating the localized dissolution of the substrate.

Hence, the low chloride concentrations (green, blue and turquoise) potentiodynamic curves, present three distinguished regions characteristic to 316LSS passive behaviour. At low potential, anodic and cathodic reactions are in competition. It is characterized by a progressive increase in current density. In this domain, the material is at its passive state. Once the potential reaches 1V (V vs SHE) the second oxidation of chromium occurs. A plateau extends up to E= 1.3 V (Vs SHE). This plateau marks the presence of a modified passive film enriched in iron. In the passive domain, the current density corresponds to the current density required to the maintenance of this passive film. Chloride concentrations are too low to cause pitting or to prevent the repassivation of the passive film. After 1.3 V vs SHE, water oxidation takes place.

The parametric study of corrosion, highlighted the role that chloride ions play in reducing the corrosion resistance of 316L SS. Increasing the chloride concentration increases the corrosion current density and reduces the extent of the passivation plateau for which the material is protected. The chloride concentration [Cl^-]= 10^{-3} M can be considered in our study conditions as a threshold value beyond it the material changes behaviour and becomes exposed to pitting corrosion, while bellow this value passivation is possible. We also concluded that 316L SS plates are extremely sensitive to the variation of the parameters pH, temperature and chloride concentration. The change of one of these parameters affects the corrosion resistance, depending on the modification of the composition and physicochemical properties of the passive film. Critical values for chloride concentrations, temperature and pH were provided ([Cl^-]= 10^{-3} M and pH =3.5 in our working conditions). As for pH, it affects directly the chemical stability of the passive film. In fact the critical pH value under which the passive film disappears and the generalised corrosion is promoted, represents a characteristic value for stainless steel known as the depassivation pH (ranged from pH 1.5 to 2 in the case of 316L) [35]. The identification of the different threshold values is important, as beyond it the plate can change from passive behaviour, to generalised corrosion or even to pitting.

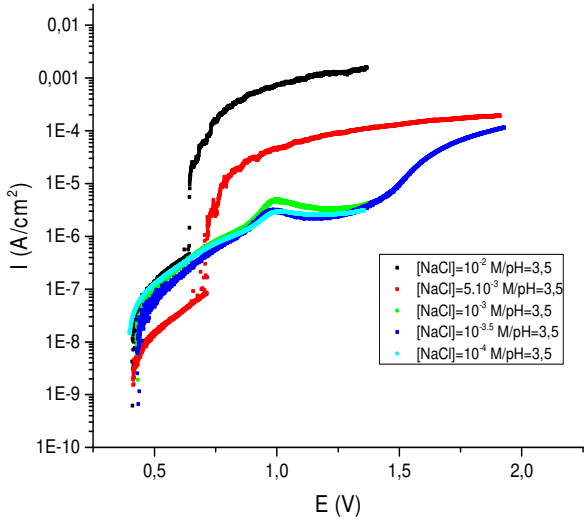

Fig. 2-Evolution of the current density with the potential for different chloride concentrations Black: [Cl^-]= 10^{-2} M; Red curve: [Cl^-]= 5.10^{-3} M; Green [Cl^-]= 10^{-3} M; Blue: [Cl^-]= $10^{-3.5}$ M; turquoise: [Cl^-]= 10^{-4}M) (V vs. SHE) (Anodic part).

All the data collected from this study are gathered in a look-up table in Matlab® taking as entries: The temperature, potential, pH and Fluoride concentration. This table can provide the current density at different PEMFC's operating conditions as explained in the section 2.3.

2.3. Corrosion Look-Up Table

This part of our work relies on a Look Up Table (LUT) generated from the experimental data, obtained by the corrosion parametric study. At the beginning, the potentiodynamic curves were smoothed by the Matlab® software which consists on effecting

background correction in order to reduce the measurement signal's noise. Later a 4D matrix is created from the smoothed data on Matlab/Simulink® software. This matrix represents the parameters of the LUT:
The inputs are: the smoothed potential values E (V vs. SHE), the Fluoride ions concentration [F^-] (M), the temperature (°C) and the pH. The equivalent variables calculated by the code use IS units and thus a unit conversion is one at the input of the LUT. The interpolation method allows the calculation of the current density for the chosen conditions of E, [F^-], T and pH. The output is the current density I ($A.m^{-2}$). Table 1 shows the data chosen to integrate the LUT from the parametric corrosion study. In addition, the Fig. 3 shows the complete structure of this LUT.

Table 1- Selected data from parametric corrosion study to integrate the LUT.

	pH				
T(°C)	**3.5**	**4**	**4.5**	**5**	**[F^-] M**
60		X	X	X	10^{-3}
	X	X	X	X	10^{-2}
70	X			X	10^{-3}
		X	X	X	10^{-2}
80	X	X	X	X	10^{-3}
	X	X	X	X	10^{-2}

In order to integrate the LUT in the PEMFC performance model, the corrosion parameters as potential, Fluoride concentration and temperature were used as system parameters.

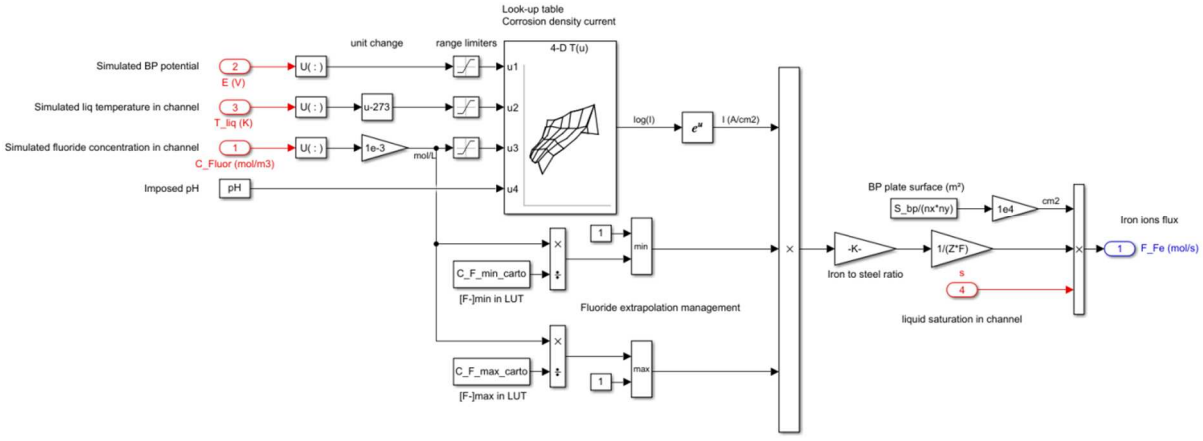

Fig. 3-Corrosion's LUT, inputs and outputs.

Briefly, some simplifications hypothesis has been taken into account:

- The plate's potential E is considered as cell potential value (E at the cathode and 0V at the anode), neglecting the potential loss in the GDL.
- The fluoride ions concentration is the concentration in the liquid water transported to channels through the GDL.
- The cell's temperature is equal to the temperature of the liquid in the channels.
- The current density given by the LUT results from the plates' corrosion and water reduction. The ionic current I is deduced from this current density multiplied by the wetted channel surface, assuming a homogeneous corrosion: $I = Jc * S_L * S_{chanel}$ where S_L is the liquid fraction and $S_{channel}$ the channel surface
- The pH values are directly injected since the code does not evaluate it locally.
- The interpolation is linear.

Once integrated in MePHYSTO, the LUT can be used outside the range of the experimental values of [F^-], in this case an extrapolation protocol is defined. In fact, the choice of the operating conditions, allows the temperature, the potential and the pH to be kept within the LUT's data range. However, the simulated [F^-] could reach values outside the LUT's data range, spatially at the beginning of the dynamic calculations where it is close to zero. Thus, a special extrapolation process has been developed outside the LUT as illustrated on the Fig. 3. When the simulated [F^-] is lower than the lowest [F^-] present in the data range, the lowest value is used as an input for the LUT. Then, the corrosion current calculated by the LUT is divided by the ratio between the two concentration $[F^-]_{simulated}/[F^-]_{lower\ bound}$. This extrapolation may seem controversial but is inevitable at the beginning of simulations (initialisation). As the corrosion current does not evolve monotonously against, [F^-] a classical linear extrapolation in the LUT is not possible.

The LUT's behaviour was validated and its efficiency confirmed. However, its sensitivity towards some parameters may present some limits which arises from:

- The effectiveness of the smoothing methods is not the same for all the curves. Indeed, one polarization curve may have 3 regions relative to different mathematical functions.
- The experimental variation relative to the uses of three cells for the potentiodynamic measurements.

As shown in the schematic representation of the LUT in Fig. 3, it gives the corrosion current density I (A/cm^2) as output. We assume that the current density is relative to the ferrous ions release. Therefore, the Faraday law is applied to deduce the ferrous ions concentration [Fe^{2+}] released by the BPs.

$$n(Fe^{2+}) = \frac{It}{ZF}dt \tag{1}$$

Where:
$n(Fe^{2+})$ is the ferrous ions molar number (mol),
I is the corrosion current (A),
t is time (s),
F is faraday constant (96485 (C/mol)),
Z is Charge number equal to 2 for ferrous ions.
The Fig. 4 is an example of the polarisation curves given by the LUT. The variation of operating conditions can change drastically the material's resistance towards corrosion. The values of the current density in case of pitting corrosion are to important which leads to the overestimation of the ferrous ions content.

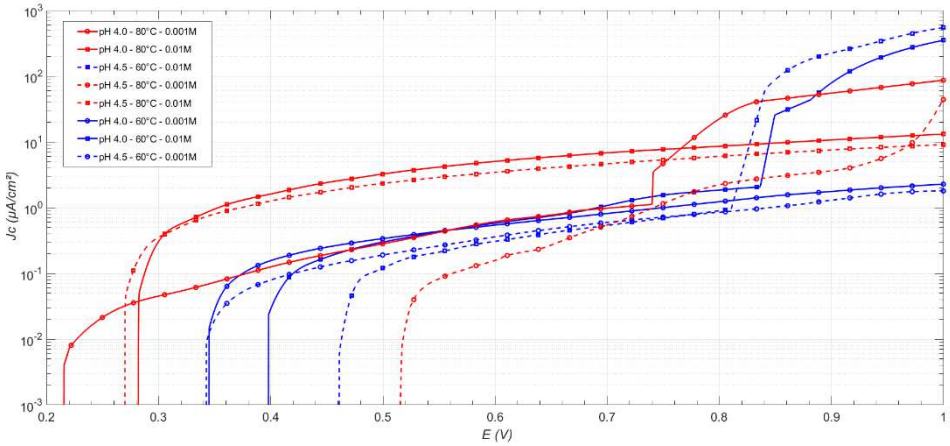

Fig. 4-Variation of the LUT's calculated current density in function of potential for different operating conditions.

3 Membrane chemical degradation model

The chemical degradation of the membrane is considered as one of the most crucial degradation phenomena affecting the performance and the durability of PEMFCs. It consists in a chemical attack on the membrane chains by hydroxyl radicals. The simultaneous presence of ferrous ions (Fe^{2+}) released by BPs' corrosion and hydrogen peroxide (H_2O_2) is responsible for the hydroxyl radicals' production, resulting in breakage of the membrane molecular chains. In the membrane chemical degradation process, H_2O_2 is considered as a forerunner, its presence is absolutely necessary. In our reaction pathway, we consider that the H_2O_2 is produced by the incomplete oxygen reduction on platinum catalyst. In fact, under PEMFC operating conditions the oxygen is reduced on the cathodic side in order to react with protons and electrons and form water. But this process takes place through two possible reaction paths: the first path is detailed in (2), and the second path is detailed in (3), where H_2O is produced through a two steps reaction. The second path is the most common, where the H_2O_2 is produced as an intermediate species [20], [36].

Path 1

$$O_2 + 4H^+ + 4e^- \rightarrow 2H_2O \tag{2}$$

Path 2

$$O_2 + 2H^+ + 2e^- \rightarrow H_2O_2 \tag{3}$$

$$H_2O_2 + 2H^+ + 2e^- \rightarrow 2H_2O$$

The kinetic of the H_2O_2 production reaction was provided by the work of Chandesris et al. ([37] [27]), the reaction rate K_1 is given by the equation (4).

$$K_1 = k_1[O_2][H^+]^2 \tag{4}$$

Where $[O_2]$ and $[H^+]$ are the concentrations of O_2 and H^+ in $mol.L^{-1}$, and the protons concentration is given by the equation (5).

$$[H^+] = \frac{\rho_{PFSA}}{EW} \tag{5}$$

Where ρ_{PFSA} and EW are respectively the humidity dependent density and the equivalent weigh of the PFSA (polyfluorinated sulfonic acid) ionomer.
While the reaction kinetic constant k1 is provided by the relation (6):

$$k_1 = k_1^0 \exp\left(\frac{-Eact_1}{RT}\right) \exp\left(\frac{-F\eta_{H_2O_2}\alpha_{H_2O_2}}{RT^0}\right) \tag{6}$$

E_{act1} is the activation energy of the of hydrogen peroxide formation's reaction,

k_1^0 takes the value of 706.810^{-14} $m^7.mol^{-2}.s^{-1}$,[27],

T^0 is the standard temperature,

$\alpha_{H_2O_2}$ is the transfer coefficient of the reaction of hydrogen peroxide formation equal to 0.5,

$\eta_{H_2O_2}$ is the equilibrium potential equal to 0.695 (V), [38]

Many publications studied the effect of H_2O_2 on membrane degradation [39] [40] [41]. Their work pointed out that the production of H_2O_2 is more significant when the membrane is thin. This effect is linked to the increase of oxygen cross over through thin membranes [20]. And it is also more important at the cathodic side, the site of the oxygen reduction reaction [42], [43]. Moreover, H_2O_2 is characterized by a relative stability and a long lifetime in the typical PEMFC's conditions. It is able to produce hydroxyl radicals detailed in the second reaction of the Table 2 responsible for the membrane chemical attack. However, it is not a strong enough oxidant, and its decomposition to free radicals $HO^{\bullet}$ and $HOO^{\bullet}$ requires the presence of ferrous ions (equations 3, 4, 5, 8 and 9 in Table 2). In the transformation of hydrogen peroxide to free radicals the ferrous ions play the role of catalyst. On their part, the free hydroxyl radicals $HO^{\bullet}$ and $HOO^{\bullet}$ attack the polymer structure at different points. In the literature different sites have been proposed as weak points likely to be subject of the free radical's attack ([44]-[45]-[46]). This mechanism causes an advanced unzipping in the membrane structure either backbones, end groups or side chains. The exact location of the attack is still a matter of debate ([47]-[48]-[49]). In our model, we assume that the hydroxyl radicals take as target the carboxylic end groups considered like a weak spot in the membrane's structure. Under severe conditions, the hydroxyl radicals' attack continues until cutting completely the junction between the membrane and the end groups and forms the so called "products" referred in equation 14 (Table 2). This attack causes the membrane thinning accompanied by the release of fluoride components. Our Fenton model calculates the concentration of different species involved in the mechanism such as hydroxyl radicals, hydrogen peroxide, ferrous and ferric ions and the fluoride released by membrane's degradation in order to follow the evolution of the degradation.

Table 2- Simulated reaction system [25].

Reaction number	Reaction equation	E_{act} / kJmol^{-1}	A / s^{-1}
1	$O_2 + H_2 + 2e^- \rightarrow H_2O_2$	42.45	-
2	$H_2O_2 \rightarrow 2HO^{\bullet}$	200	1.09×10^{25}
3	$H_2O_2 + Fe^{2+} \rightarrow Fe^{3+} + HO^{\bullet} + HO^-$	35.4	1.03×10^{08}
4	$H_2O_2 + Fe^{3+} \rightarrow Fe^{2+} + HOO^{\bullet} + H^+$	126	4.76×10^{17}
5	$HO^{\bullet} + Fe^{2+} \rightarrow Fe^{3+} + HO^-$	9	9.46×10^{09}
6	$HO^{\bullet} + H_2O_2 \rightarrow HOO^{\bullet} + H_2O$	14	1.53×10^{11}
7	$HO^{\bullet} + O_2 \rightarrow HOO^{\bullet} + H_2O$	-	2.4×10^{11}
8	$H_2O_2 + Fe^{3+} \rightarrow Fe^{2+} + HOO^{\bullet} + H^+$	33	1.21×10^{10}
9	$HOO^{\bullet} + FeFe^{3+} + H^+ \rightarrow Fe^{2+} + O_2 + H^+$	42	2.74×10^{13}
10	$HOO^{\bullet} + H_2O_2 \rightarrow HO^{\bullet} + H_2O + O_2$	30	1×10^{7}
11	$2HOO^{\bullet} \rightarrow H_2O_2 + O_2$	20.6	1.05×10^{12}
12	$HO^{\bullet} + HO^- \rightarrow H_2O_2$	7.9	1.31×10^{11}
13	$HOO^{\bullet} + HO^{\bullet} \rightarrow H_2O + O_2$	14.2	2.09×10^{12}
14	$HO^{\bullet} + R_f - CF_2 - COOH \rightarrow products$	6.5	1.35×10^{07}

The initial concentration of the end group [Rf-CF_2-COOH] has been taken equal to 200 as suggested by Gubler *et al.* [50]. Our kinetic framework and the assumptions of the model are based on spread knowledge across several chemical and technical publications. At the same time simplification hypothesis have been considered. The first equation for the H_2O_2 production is implemented in the GDE sub-model (Gas Diffusion Layer/Microporous layer/ Catalyst Layer) (Table 2) and all the other 13 equations are solved in the membrane block. The oxygen, hydrogen and water concentrations in the membrane requested by these equations are calculated locally from local molar balance and permeation flux. The reaction 14 describing the emission of fluoride is considered as a macroscopic reaction which behaves like an elementary reaction. For some of the reaction mentioned in Table 2, the literature did not offer enough data for the reaction constant rates at 353 K, so the temperature dependency of these reactions rates were calculated by the Arrhenius law (7).

$$K = A \cdot \exp\left(\frac{E_{act}}{R \cdot T}\right) \quad (7)$$

where K is the rate constant in s^{-1},
A, the frequency factor in s^{-1} (also known as the pre-exponential factor),
E_{act} the activation energy in $Jmol^{-1}$,
R the gas constant in $Jmol^{-1}K^{-1}$,
and T the temperature in K.
The rate constant for equation 2 "K_2" has been calibrated according to the test with no initial ferrous ions. The values for K_4 and K_5 relative to equations 4 and 5 came from the Futter *et al.* publication [51]. While the values of K_6, K_7, K_{10} and K_{11} have been fitted using all the tests described in the validation part (3.1) . From the set of the 14 coupled equations, we build a system of coupled differential equations, this system is solved in order to obtain the time evolution of all participating chemical species. The equation (8) allows the calculation of the different species' concentrations in the membrane considered as the volume control for the balances:

$$\frac{d[C_S]}{dt} = \sum_{reaction,i} (\nu_{S,in} . R_i) + \nu_{S,in} - \nu_{S,out} \quad (8)$$

ν_s is the stoichiometric factor of species s in reaction i,
R_i the reaction rate in $mol.m^{-3}s^{-1}$,
and $\nu_{S,in}$ and $\nu_{S,out}$ are respectively the volumetric flow rate for the species F^-, Fe^{2+}, H_2, O_2 and H_2O crossing the membrane. The other species involved in the equations (as $HO^{\cdot}$ and $HOO^{\cdot}$…) are considered as present only in the membrane.

3.1. Model validation

In order to inspect the response of the model and validate its performance, experimental data are required. For this step, the Fenton test is considered as a reference test in the membrane degradation study. Generally, it is an *ex-situ* test which consist in exposing the membrane to a mixture of hydrogen peroxide (H_2O_2) and ferrous salts at PEMFC functioning temperature (from 333 K to 363 K) and following the fluoride release with time [15]. In this model validation process, data was provided by our collaborators Steffen Frensch from Aalborg University [52] and Nada Zamel from the Fraunhofer Institute of Solar Energy Systems (ISE). The tests carried out in the ISE use constant H_2O_2 concentration and variable Fe^{2+} concentrations, as for Frensch *et al.* the ratio of $[H_2O_2]/[Fe^{2+}]$ was variated. For both cases, the fluoride content was measured by an ion selective electrode (ISE, Hach device ISE301F and MM374). The experimental set up is detailed in Table 3. Two polyfluorinated sulfonic acid (PFSA) membranes have been discussed: Nafion® XL and Nafion® 115. These membranes are widely used as reference materials for degradation tests because of their good chemical robustness and their high proton conductivity.

Table 3. Fenton test experimental setups.

Sources	Test	$[H_2O_2]$ (Wt %)	$[Fe^{2+}]$ (ppm)	Temperature (K)	Membrane
A Steffen Frensch [53]	1(A)	0	0	353	Nafion® 115
	2(A)	0	1		
	3(A)	0.003	1		
	4(A)	0.03	1		
	5(A)	0.3	1		
	6(A)	3	1		
	7(A)	30	1		
	8(A)	3	0		
	9(A)	3	0.1		
	10(A)	3	10		
	11(A)	3	20		
B ISE		30	2	353	Nafion® XL
			4		
			6		
			8		
			10		
			12		

In order to mimic the accelerated *ex-situ* tests conditions, the first equation of the Fenton model responsible for the hydrogen peroxide production is not taken into account in the model. Thus, the instantaneous concentration of H_2O_2 depends on its initial concentration and on the consumption from the overall Fenton process. The model has been extracted from the PEMFC code used to as a standalone model with initial boundary conditions. It considers the diffusion of species between the solution and the membrane, represented as a coupled two-component system with different concentrations calculated by a molar balance. The diffusive flux of all the ions involved in the mechanisms (fluorides, iron…) between the membrane and the solution are modelled by the Fick law. The diffusion flux is estimated using a coarse two-node scheme (one in the solution and one in the membrane). The diffusion coefficients for all the species participating in the Fenton mechanism were also determined in Nafion, the different values are gathered in Table.4.

Table.4-The diffusion coefficients at 353 K.

Species	Diffusion coefficient (m^2/s)	Source
HO°	6.8×10^{-11}	[51]
HOO°	3×10^{-9}	[51]
Fe^{2+}	3.67×10^{-10}	Calculated ([54])
Fe^{3+}	5.37×10^{-11}	Calculated ([54])
H_2O_2	1.6×10^{-10}	[51]
F^-	1.5×10^{-10}	[54]
O_2	2.4×10^{-11}	[51]

First, the test 7(A) (Table 3) is taken as a reference to evaluate the efficiency of the diffusion modelling. The comparison of the simulated and experimental data response in the Fig. 5(a) proves the efficiency of the diffusion's consideration between the membrane and the solution. At the beginning of the test, a clear distinction between the concentrations of the membrane and the solution is noted and in ten hours the equilibrium is reached. Nevertheless, this time scale seems to be underestimated compared to the measured and simulated fluoride concentrations in the solution. This tendency is probably relative to the coarse discretization of the diffusion. And the Fig. 5(b) relative to data **A** shows the variation of the fluoride concentration after 72 hours testing, in function of different $[Fe^{2+}]/[H_2O_2]$ ratios. It underlines how the model globally captures the dynamic of fluoride's emission for the whole range of Fe^{2+} and H_2O_2 concentrations, except beyond 10 ppm of Fe^{2+} where, surprisingly, the fluorides concentration decreases.

a b

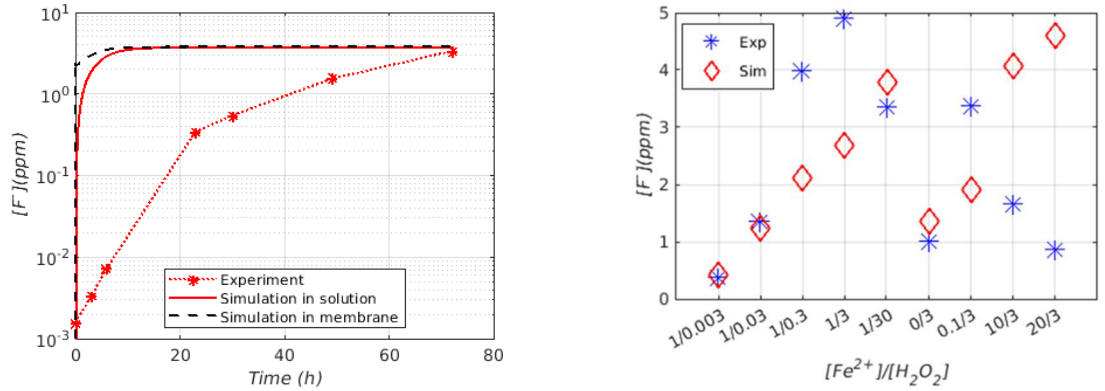

Fig. 5- Comparison of experimental data (A) and modelling results (a): Temporal evolution of fluoride content for test 7(A), (b) Final fluoride concentration evolution over $[Fe^{2+}]/[H_2O_2]$ ratio.

In order to distinguish the impact of H_2O_2 and Fe^{2+} ions on the final fluoride content, Fig. 6(a) and Fig. 6(b) were drawn. Fig. 6(a) shows the sensitivity of the model towards the of H_2O_2 evolution (at $[Fe^{2+}]$ = 1 ppm), for the whole range of H_2O_2 concentration, the model clearly captures the monotonous increases of the fluoride ions' concentration. However this tendency is less remarkable in the Fig. 6(b) relative to the evolution of fluoride ions concentration under the effect of ferrous ions increase (at $[H_2O_2]$=3% (Wt)).

a **b**

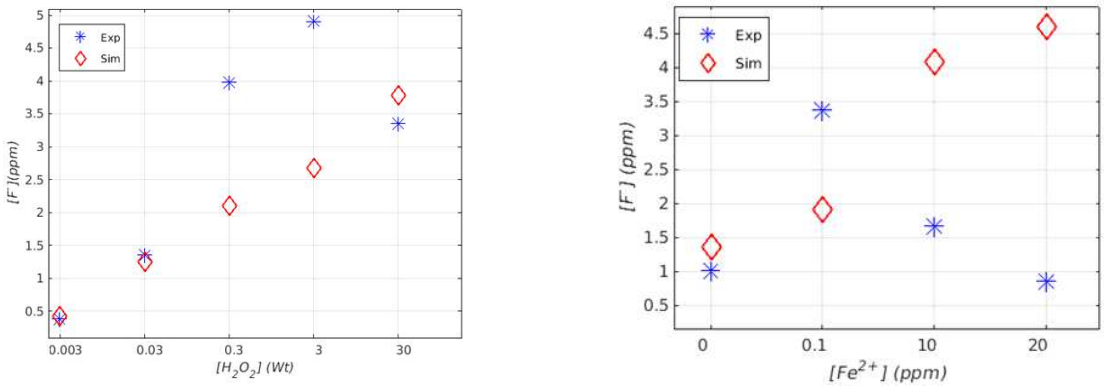

Fig. 6-Final fluoride concentration evolution : (a) over $[H_2O_2]$ (for constant $[Fe^{2+}]$) variation and (b) $[Fe^{2+}]$ variation (for constant $[H_2O_2]$), data (A). Exp: Experimental results. Sim: Simulation results.

Second, the test 3(B) was taken also as a reference. The results are presented in the Fig. 7 (a). This figure shows the temporal evolution of the fluoride concentration and leads us to think that the diffusion's time scale is probably underestimated. While the Fig. 7 (b), proves that the model captures both the order of magnitude of the fluoride concentrations as well as their rising evolution in function of the initial ferrous ions concentration.

a **b**

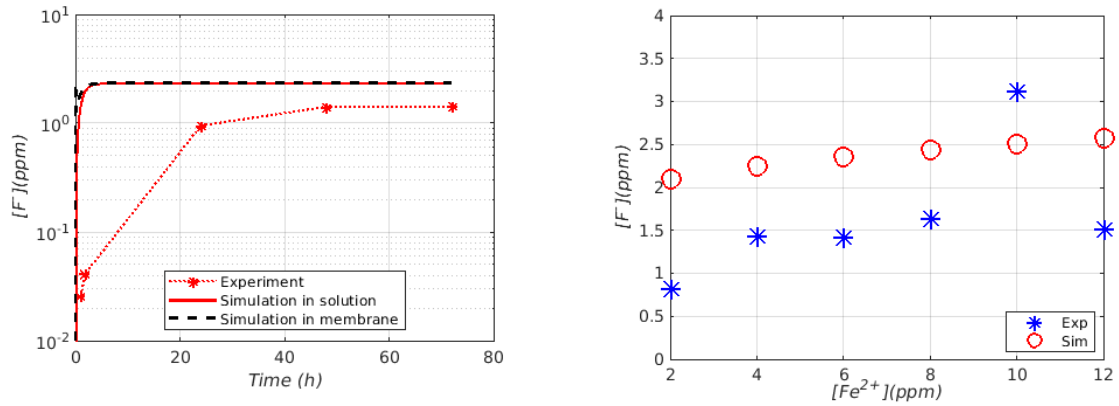

Fig. 7- Comparison of experimental data (B) and simulation results : (a) Temporal evolution of fluoride content for test 3(B), (b) Final fluoride concentration evolution over ferrous ions concentration for constant Hydrogen peroxide (30%wt).

To conclude on this part, the Fenton mechanism modelled in MePHYSTO always apprehends the order of magnitude of the F^- concentrations as well as the main evolution in function of Fe^{2+} and H_2O_2 initial concentrations. A behavior observed at high Fe^{2+} concentration present in both tests A and B will need further investigation. Our model based on Fenton kinetics provides a regular increase of the fluoride emission relative to the increase of the Fe^{2+} concentration. Whereas, an opposite behaviour is observed on the experimental data, the measured F^- concentration is lower than the registered values for inferior Fe^{2+} concentrations. This behavior was observed on Fig. 7(b) and Fig. 7 (b) respectively at $[Fe^{2+}]$ = 10 and 20 ppm for tests A and 12 ppm for tests B. The results provided by this model are sufficient to be used in the coupling process.

4 Ionic transport modelling

Once ferrous ions are released by corrosion, they are transported through gas diffusion layer (GDL), microporous layers (MPL) and catalyst layer (CL), till reaching the membrane. In the performance model, all the porous layers including GDL, MPL and CL are modelled together for the transportation. When they reach the membrane, the Fe^{2+} ions get involved in the membrane degradation process through the Fenton mechanism. The membrane degradation process is evaluated by the F^- ions' release. Once prone to degradation, the membrane starts to liberate fluoride ions, which will be transported oppositely to the Fe^{2+} to reach the BPs.
An ionic species transport law was integrated in MePHYSTO as illustrated schematically in Fig. 8. The figure represents the cathodic side of the cell. The cell is modelled vertically, as three compartments: the channel area, the GDE and the membrane. It is represented horizontally, by three connected identical meshes in plane, where the number of meshes could be increased. The same model has also been implemented on the anodic side. The modelled transport mechanisms and the simplifications hypothesis are the followings:

- Along the channels, all the ions (ferrous and fluorides) are convected by the liquid water (green arrows) using 1D discretization, the in-plane flux is neglected in the membrane and in the GDE.
- The balance of charges is not considered.
- Through the GDE, the ions are transported by convection through the liquid water and their diffusion in liquid water bridges (blue arrows) for simplification reasons the migration was not considered.
- The biggest difficulty in this modelling part, arises when no liquid water is present in the GDE or in the channels since the concentrations become infinite. To overcome these difficulties some considerations were taken into account: The liquid saturation has a bottom limit, a minimum value very close to zero (10^{-5}).

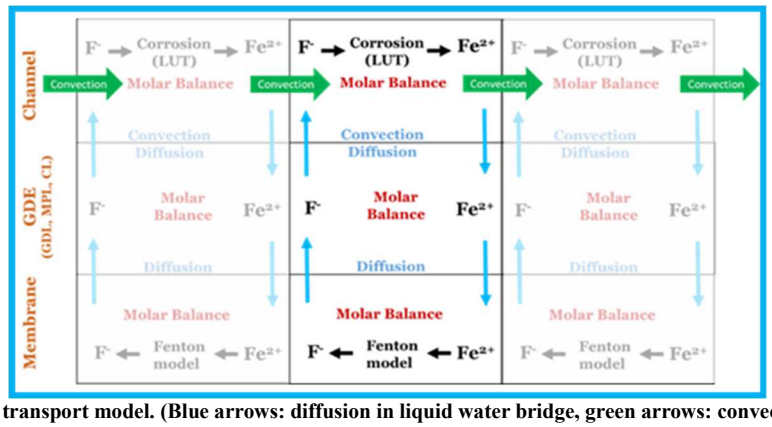

Fig. 8-Ionic species transport model. (Blue arrows: diffusion in liquid water bridge, green arrows: convection in-plane)

- The membrane is simply modelled with a molar balance equation through the overall membrane for each species assuming a spatial homogeneity of their concentration.
- The water crossing is modelled using diffusion and electro-osmosis law.

The general ionic species transport flux is given by the equation (9). The first term corresponds to the diffusive flux through the GDE and the second term corresponds to the convective flux in both channels and GDE.

$$F_i(x) = -D_{i/water}\frac{\partial C_i(x)}{\partial(x)} + \frac{C_i V(x)}{S} \quad (9)$$

i is the ionic species Fe^{2+} or F^- ions,
F_i: the flux of the ionic species,
$D_{i/water}$: the ionic species diffusion coefficient in water calculated at 353 K.
C_i: the ionic species concentrations,
S: the exchange surface between the channel and GDE or membrane and GDE for a single mesh.
The diffusion coefficient of ionic species in water at T = 353 K was calculated by the Stokes-Einstein equation (10).

$$D_{i/water} = \frac{k_B T}{6\pi\eta R} \quad (10)$$

k_B: Boltzmann constant,
T: Temperature in Kelvin,
R: Hydrodynamic radius,
η: Viscosity of water at T.

5 Coupling model results

5.1. Approach testing

Our coupling approach has the objective of binding the two main bricks of our work: the BP's corrosion and the membrane chemical degradation using the ionic species' transport. This approach offers a global view of the PEMFC's degradation process through the fluoride ions release and the membrane thinning under BP's corrosion conditions. Before starting the simulations some initial parameters are integrated in the model. This information is relative to the different species initials concentrations, the membrane and the bipolar plates characteristics as well as the cell's operating condition like inlet temperature T, global pH, inlet relative humidity and outlet pressure P, etc… The Table 5 represents an overview of some of these initial parameters.

Table 5- Overview of the initial parameters used by the model.

	Model parameter	Value
Initials concentrations (ppm)	$[O_2]_0$	0
	$[H_2]_0$	0
	$[H_2O_2]_0$	0
	$[Fe^{2+}]_0$	0
	$[Fe^{3+}]_0$	0
	$[F^-]_0$	0
Single cell	Bipolar plates' dimension	25 cm^2
	Bipolar plates' material	316L SS
Operating conditions	pH	4
	T	333 K
	P	1.5 bar
	Relative humidity anode and cathode	90%
Membrane characteristics	Stoichiometry H_2/O_2	1.2/1.8
	Type	Nafion 115
	EW	1100

As shown in Table 5, the initial concentrations of F^-, H_2O_2 and Fe^{2+} are equal to zero. During the simulation the ferrous ions will be generated by the corrosion, the H_2O_2 will be generated by the reaction 1 in Fenton mechanism (Table 2). The fluoride will be generated as a product of the membrane degradation.
Concerning the current, the simulation consists on maintaining stable the applied current at 0.2A/cm^2 for 100 hours, in order to obtain a high cell's potential (0.78 V) that promotes corrosion. We discretize the in-plane channels using 3 meshes. All the plotted results correspond to the central mesh. The liquid fractions simulated and used to calculate the concentrations are quite constant from inlet to outlet and equal to 0.75 in the membrane (water content is about 15.5) and to 5.10^{-5} in the channels (above the minimum numerical limit), making a ratio of 15000 between membrane to channel liquid fractions.
The Fig. 9 gives the evolution of the current density with time. The corrosion current density increases rapidly for the first hours from zero up to 10^{-8} A/cm^2 and then increases progressively until reaching 10^{-7} A/cm^2.

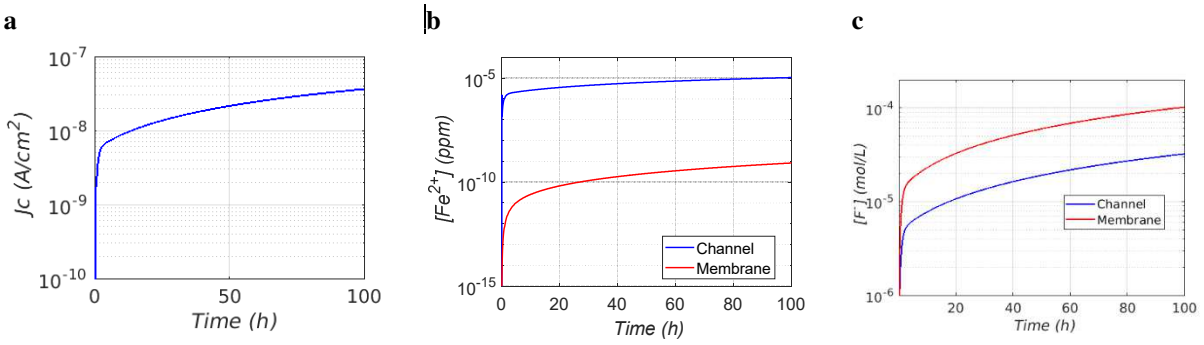

Fig. 9-(a)Variation of the corrosion current density on the cathodic side of the bipolar plate over time. (b) and (c) Evolution of the $Fe^{2+}$and F^- concentrations over time in the membrane (Red curve) and the channels on the cathodic side of the bipolar plates (Blue curve).

Relatively to the current density tendency given in the Fig. 9(a), we follow the evolution of the Fe^{2+} concentration in the BPs channels' level and in the membrane represented in the Fig. 9(b). The two curves tendencies are similar with a rapid raise at the beginning followed by a more stabilized increase. During the 100 hours' simulation time, $[Fe^{2+}]$ is more important at the BP's channels compared to the membrane, which is coherent since the Fe^{2+} are sourced by the BPs' corrosion. While at the membrane, Fe^{2+} are consumed by the Fenton mechanism. Moreover, this discrepancy in orders of magnitude could also be attributed to the difference in the water fraction between the membrane in the channels. It is close to 1 in the membrane and 10^{-5} in the channels. As shown in the Fig. 9(c), the evolution of the F^- concentration over time in the BPs' channels and the membrane have a similar dynamic to the Fe^{2+}. The concentrations in the membrane and the channels are very close, it reaches 10^{-4} mol/L in the channel which is in the range of the LUT values.

To conclude on this part, all the concentrations calculated start at zero and increase very strongly for the first hours, reaching a slightly rising plateau. The liquid saturation is constant during all the 100h of simulation. Thus, the dynamic of the ionic species concentrations is fully induced by the Fenton dynamic and not by the liquid water saturation's evolution between the channels and the membrane.
The ionic transport model has shown its efficiency since the iron and the fluoride ions are transported through the GDE. The ferrous ions' transport from the channel to the membrane is mainly driven by diffusion. While the fluoride ions transport is driven by convection since the liquid flux in the cathodic side is oriented mainly from the membrane to the channel. Thanks to the ionic transport model, the corrosion dynamic is synchronized with the Fenton process.

5.2. Simulation of the NEDC cycle

In order to assess the model's capabilities and evaluate its response to operating conditions variations, a standard automotive cycle has been simulated. This Fuel Cell Cycle is based on the "New European Driving" Cycle (NEDC). The NEDC is used for type approval of light-duty vehicles and features periods of acceleration, deceleration and constant speed. It consists of four repetitions of a low speed urban cycle of 195 seconds each followed up by a part which simulates a motorway (highway) driving cycle of 400 seconds duration. That is equivalent to a theoretical distance of approximately 11 km driven in about 20 minutes [55]. The NEDC cycle has been implemented in MePHYSTO and simulated using a coarse discretization of 3 meshes. The Table 6, regroups the simulation condition inspired from the cycle.

Table 6- NEDC Cycle Simulation condition

	Model parameter	value
Initials concentrations (ppm)	$[O_2]_0$	0
	$[H_2]_0$	0
	$[H_2O_2]_0$	0
	$[Fe^{2+}]_0$	0
	$[Fe^{3+}]_0$	0
	$[F^-]_0$	0
Single cell	Bipolar plates' material	316L SS
	Number of Anodic channels	10
	Number of Cathodic channels	20
Operating conditions	BP's Surface	612 cm^2
	Active layers' Surface	350 cm^2
	pH	4

	T	353 K
	P	1.5 bar
	Relative humidity/Anode	50%
	Saturation Pressure/Anode	2.5
	Relative humidity/Cathode	30%
	Saturation Pressure / Cathode	2.3
	Stoichiometry H_2/O_2/Anode	1/0
	Stoichiometry H_2/O_2/Cathode	0/0.21
Membrane characteristics	Type	Nafion 112
	EW	820
	Thickness	15 µm

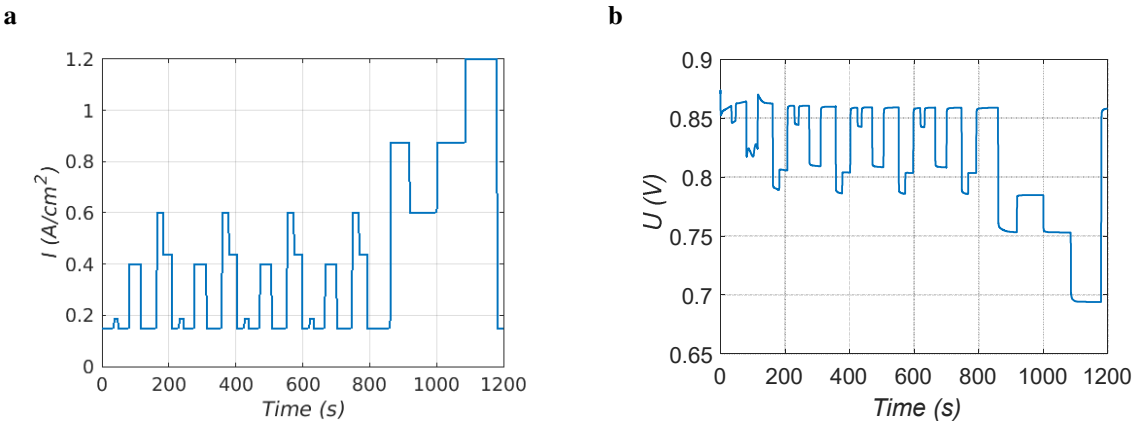

Fig. 10- (a)The cell's applied current density and (b) The resulting cell potential.

The Fig. 10(a) represents the cell's current density during the cycle. The maximum current density has been chosen in order to induce a cell's voltage favorable to corrosion conditions. The corresponding cell voltage is plotted on the Fig. 10(b).
The calculated corrosion current density on the cathodic channel is represented on Fig. 11(a). At the beginning of the cycle this current density is equal to zero, since the concentration of the fluoride ions is initialized at zero. The establishment of the corrosion is followed by the progressive increase of the corrosion current density. Then, this current density varies over a wide range of one order of magnitude during the rest of the cycle accordingly to the cell potential and thus to the imposed current.

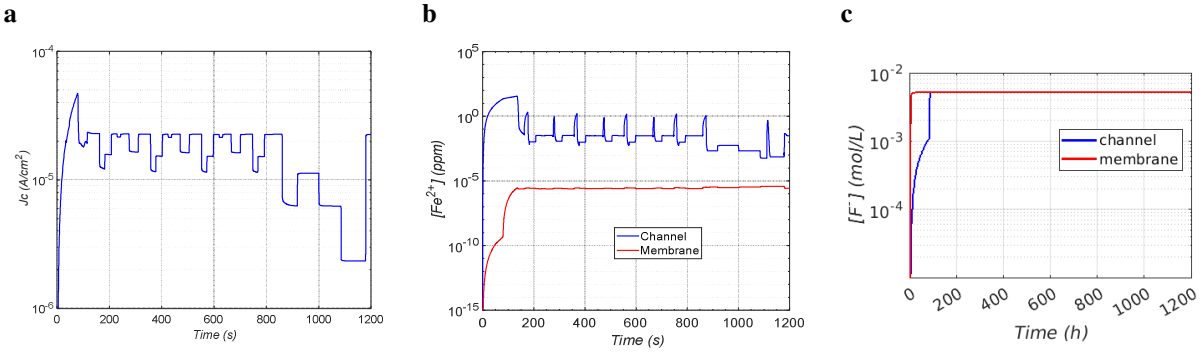

Fig. 11-(a)Variation of the corrosion current density, (b) and (c) Variation of Fe^{2+} and F^- concentrations on the cathodic side at the channel (Blue line) and Membrane (Red line).

The Fig. 11(b) shows the variation of Fe^{2+} ions concentration in the channel (blue curve) and the membrane (red curve). The amount of Fe^{2+} fluctuates more in the channel compared to the membrane due to the diffusion from channel to membrane that smooths the concentration. The comparison between the concentrations, indicates that it remains below 10^{-5} ppm in the membrane, far from the classical 1 to 10 ppm used in *ex-situ* experiments. While in the channel it is around 10^{-2} ppm. Due to the diffusion, the concentration of Fe^{2+} in the membrane rises slightly later compared to the concentration in the channel at the beginning of the cycle. The fluoride ions' concentration in the channel and the membrane are represented in the Fig. 11(c). This concentration rises from zero to a high value at the beginning of the cycle when the

Fenton and the corrosion models start to interact strongly. Finally, it reaches a high value: $[F^-] \sim 10^{-2}$ mol/L, which corresponds to the maximum value used in the corrosion parametric study. The channel concentration rises slightly compared to the one in the membrane at the beginning of the cycle, this delay is relative to the diffusion process.
During the cycle, the concentrations of F^- in the channel and the membrane are very close, however the blue curve reached the plateau with a delay. This behavior is relative to the lack of liquid water in the cell during this period and consequently a low ionic transport efficiency. The expected tendency would be a more important concentration at the membrane since it represents the source of the fluoride in the cell environment. This tendency is explained by the difference of liquid volume between the membrane and the channel as shown in Fig. 12**.** It represents the evolution of the water content in the membrane and the liquid fraction in the channel.

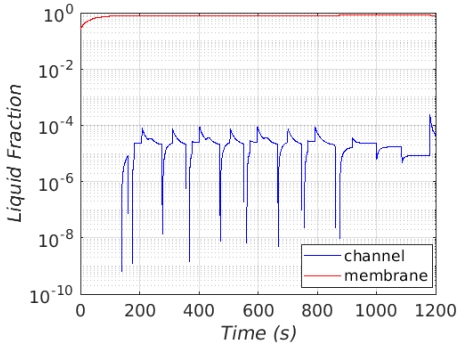

Fig. 12-Variation of liquid water fraction over time.

The observation of Fig. 12 leads to the conclusion that the variation of Fe^{2+} at the channel and the membrane is mainly generated by the fluctuation of the liquid water evolution.
The presented results confirm the efficiency of the coupling approach. The evolution of the ionic species concentration as fluoride ions relative to membrane degradation and ferrous ions relative to bipolar plates corrosion are interdependent and follow the cycle implication. However, the given order of magnitudes has to be confirmed with further experimental data based on waste PEMFC water after the cycling or based on more sophisticated *in-situ* measurements.

Conclusion

In this study we followed the corrosion of 316L SS plates under simulated fuel cell conditions. 316L SS exhibit passive state or pitting corrosion as it could be damaged by fluoride. The collected data is stored in a 4D Matlab LUT and connected to the MePHYSTO code that simulates the performances and the degradations of PEM fuel cells in order to determine the Fe^{2+} contents relative to BPs' corrosion. The membrane chemical degradation is modelled based of the kinetics of the Fenton mechanisms. The model was validated through two independent sets of *ex-situ* tests. The convection/diffusion model for fluorides and iron ions through the GDE and along the channels has been implemented in the code. It drives the transport of fluorides generated by the membrane's degradation to the channel, where they enhance the BPs' corrosion. It also transports the Fe^{2+} generated by the corrosion in the channels to the membrane where they catalyze the Fenton process. The coupling of the two degradation models via the transport model allows the evaluation of synergism effect between the membrane and the BPs' degradations. Different simulations based on constant current and automotive NEDC cycle, have shown the capability of the code to estimate the evolution of BPs' corrosion and membrane degradation with time. The results confirmed the interest and the efficiency of the approach of coupling these two phenomena. The first results, privileges the track that the Fe^{2+} concentrations used in the conventional *ex-situ* tests are overestimated.

Appendix

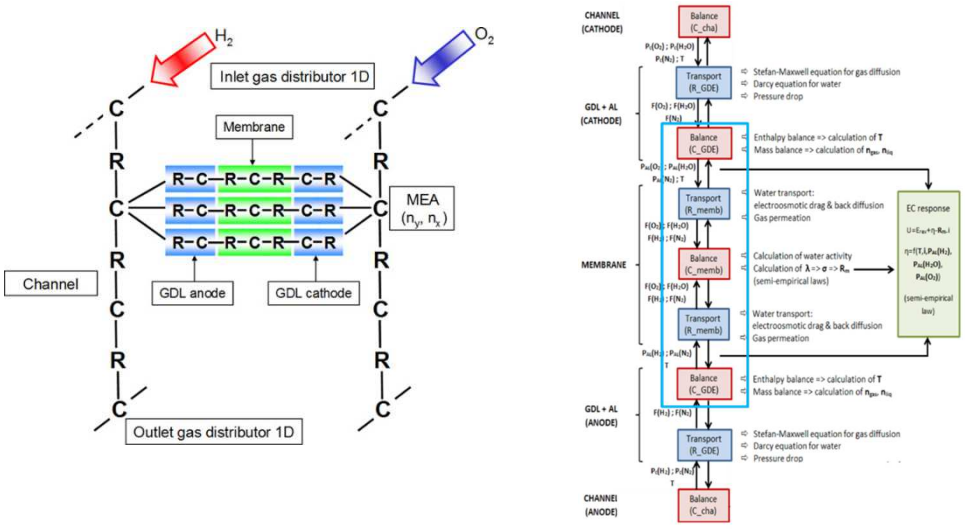

Fig. 13- The MePHYSTO code: left: the overall model, right: the through plane discretization. Red blocks correspond to balance (C) equations for all the involved species. The blue blocks (R) correspond to molar flux calculations.

The MePHYSTO-FC code gives the cell's voltage as a function of operating conditions such as current, temperature, relative humidity, oxygen and hydrogen partial pressures. MePHYSTO is based on a lumped pseudo Bond Graph approach[30], [33], [56]-[61] and implemented in Matlab/Simulink®. It uses elementary resistive blocks (R) and capacitive blocks (C) by analogy with electrical circuits. The resistive blocks (R) calculate the flows and the heat flux. The capacitive blocks (C) solve molar and enthalpy balances. The whole cell model is described on the left side of the Fig. 13. The two vertical chains of R-C blocks correspond to the channel modelling. In the C blocks the molar and enthalpy balances are solved for gases, vapor and liquid water assuming thermal equilibrium between phases. The R blocks solve a closure law (flows are proportional to pressure variations induced by the heat loss) for gas and liquid phases assuming that the pressures of the two-phase are equal. In the present figure, the channels are modelled using a 1D discretization but, in the case of a complex geometry such as serpentine plates, a 2D discretization can be used. Through-plane, the discretization is summarized on the left side of the Fig. 13 and detailed on the right one. In the through-plane direction, the discretization is 1D using one group R-C-R for the membrane and two R-C groups for the cathodic and anodic GDE. The GDE model includes only the GDL (Gas Diffusion Layer) and the MPL (MicroPorous Layer). The CL (Catalyst Layer) is not discretized. The overpotential and the reversible potential are calculated at the interface between the cathodic GDE and the membrane. The ohmic losses are calculated for every component including the membrane where a semi-empirical law, originated from the Springer model, is fitted on experimental data. The reversible potential is calculated using the classical thermodynamic laws while the overpotential is calculated using a semi-empirical law deduced from the Butler-Volmer equation and simplified using coefficients that are fitted from polarization curves. Concerning the fluid transports: gas (including vapor) diffusion is modelled in the GDE using the Stefan–Maxwell's Law, liquid water is transported using the Darcy two-phase flow model and the capillary pressure is calculated using the Leveret function. The liquid flow through the membrane is calculated using the diffusion and osmotic drag models. The gas permeation through the membrane is also considered.

Acknowledgments

This research was financially supported by ARC Energies Rhone Alpes. The authors would like also to acknowledge data support offered by our collaborators Nada Zamel and Sebastian Prass from Fraunhofer Institute of Solar Energy Systems (ISE) and Steffen Frensch. And finally we provide our sincere acknowledgments to Frederic Fouda-Onana and Pascal Shott for their scientific input and significant support.

REFERENCES

[1] COP21 de Paris : le résumé des enjeux et des engagements pris par les Etats. Selectra 2018. https://selectra.info/energie/guides/environnement/cop21.
[2] Technology Roadmap - Hydrogen and Fuel Cells – Analysis. IEA n.d. https://www.iea.org/reports/technology-roadmap-hydrogen-and-fuel-cells.
[3] DOE Technical Targets for Fuel Cell Systems and Stacks for Transportation Applications. US DOE's Fuel Cell Technologies Office Multi-Year Research, Development, and Demonstration Plan - 34 Fuel Cells n.d. https://www.energy.gov/eere/fuelcells/doe-technical-targets-fuel-cell-systems-and-stacks-transportation-applications.
[4] The Global Fuel Cell Market: Size, Share & Trends Analysis by Product, Application and Region (2018-2025) - Projected to Grow at a CAGR of 20.9% - ResearchAndMarkets.com 2018. https://www.businesswire.com/news/home/20181204005535/en/Global-Fuel-Cell-Market-Size-Share-Trends.
[5] de Bruijn FA, Dam VAT, Janssen GJM. Review: Durability and Degradation Issues of PEM Fuel Cell Components. FUEL CELLS 2008:20.
[6] J. Wu, X Z.Yuan, JJ.Martin,H.Wang, J.Zhang,J.Shen, S.Wu et W.Merida.,. A review of PEM fuel cell durability: Degradation mechanisms and mitigation strategies. Journal of Power Sources 2008;184:104–19. https://doi.org/10.1016/j.jpowsour.2008.06.006.
[7] Wu J, Yuan XZ, Martin JJ, Wang H, Zhang J, Shen J, et al. A review of PEM fuel cell durability: Degradation mechanisms and mitigation strategies. Journal of Power Sources 2008;184:104–19. https://doi.org/10.1016/j.jpowsour.2008.06.006.
[8] Hermann A, Chaudhuri T, Spagnol P. Bipolar plates for PEM fuel cells: A review. International Journal of Hydrogen Energy 2005;30:1297–302. https://doi.org/10.1016/j.ijhydene.2005.04.016.
[9] Zatoń M, Rozière J, J. Jones D. Current understanding of chemical degradation mechanisms of perfluorosulfonic acid membranes and their mitigation strategies: a review. Sustainable Energy & Fuels 2017;1:409–38. https://doi.org/10.1039/C7SE00038C.
[10] Lavigne O, Alemany-Dumont C, Normand B, Berthon-Fabry S, Metkemeijer R. Thin chromium nitride PVD coatings on stainless steel for conductive component as bipolar plates of PEM fuel cells: Ex-situ and in-situ performances evaluation. International Journal of Hydrogen Energy 2012;37:10789–97. https://doi.org/10.1016/j.ijhydene.2012.04.035.
[11] Wang Y, Northwood DO. An investigation into TiN-coated 316L stainless steel as a bipolar plate material for PEM fuel cells. Journal of Power Sources 2007;165. https://doi.org/10.1016/J.JPOWSOUR.2006.12.034.
[12] Ren YJ, Zeng CL. Corrosion protection of 304 stainless steel bipolar plates using TiC films produced by high-energy micro-arc alloying process. Journal of Power Sources 2007;171:778–82. https://doi.org/10.1016/j.jpowsour.2007.06.075.
[13] Liu M, Wang C, Xie F, Mao Z. A polymer electrolyte fuel cell life test using accelerating degradation technique. International Journal of Hydrogen Energy 2013;38:11011–6. https://doi.org/10.1016/j.ijhydene.2013.02.086.
[14] Khorasany RMH, Singh Y, Sadeghi Alavijeh A, Kjeang E, Wang G, Rajapakse N. Fatigue properties of catalyst coated membranes for fuel cells: Ex-situ measurements supported by numerical simulations. International Journal of Hydrogen Energy 2016. https://doi.org/10.1016/j.ijhydene.2016.04.042.
[15] Yuan X-Z, Li H, Zhang S, Martin J, Wang H. A review of polymer electrolyte membrane fuel cell durability test protocols. Journal of Power Sources 2011;196:9107–16. https://doi.org/10.1016/j.jpowsour.2011.07.082.
[16] Kundu S, Fowler MW, Simon LC, Abouatallah R, Beydokhti N. Degradation analysis and modeling of reinforced catalyst coated membranes operated under OCV conditions. Journal of Power Sources 2008;183:619–28. https://doi.org/10.1016/j.jpowsour.2008.05.074.
[17] Yuan XZ, Wang H, Zhang J, Wilkinson DP. Bipolar Plates for PEM Fuel Cells - From Materials to Processing 2005:12.
[18] Tawfik H, Hung Y, Mahajan D. Metal bipolar plates for PEM fuel cell—A review. Journal of Power Sources 2007;163:755–67. https://doi.org/10.1016/j.jpowsour.2006.09.088.
[19] Lechartier E, Laffly E, Péra M-C, Gouriveau R, Hissel D, Zerhouni N. Proton exchange membrane fuel cell behavioral model suitable for prognostics. International Journal of Hydrogen Energy 2015;40:8384–97. https://doi.org/10.1016/j.ijhydene.2015.04.099.
[20] Frühwirt P, Kregar A, Törring JT, Katrašnik T, Gescheidt G. Holistic approach to chemical degradation of Nafion membranes in fuel cells: modelling and predictions. Phys Chem Chem Phys 2020;22:5647–66. https://doi.org/10.1039/C9CP04986J.

[21] Jahnke T, Futter G, Latz A, Malkow T, Papakonstantinou G, Tsotridis G, et al. Performance and degradation of Proton Exchange Membrane Fuel Cells: State of the art in modeling from atomistic to system scale. Journal of Power Sources 2016;304:207–33. https://doi.org/10.1016/j.jpowsour.2015.11.041.
[22] Xie T, Hayden CA. A kinetic model for the chemical degradation of perfluorinated sulfonic acid ionomers: Weak end groups versus side chain cleavage. Polymer 2007;48:5497–506. https://doi.org/10.1016/j.polymer.2007.07.043.
[23] Burlatsky SF, Gummalla M, O'Neill J, Atrazhev VV, Varyukhin AN, Dmitriev DV, et al. A mathematical model for predicting the life of polymer electrolyte fuel cell membranes subjected to hydration cycling. Journal of Power Sources 2012;215:135–44. https://doi.org/10.1016/j.jpowsour.2012.05.005.
[24] Wang H, Sweikart MA, Turner JA. Stainless steel as bipolar plate material for polymer electrolyte membrane fuel cells. Journal of Power Sources 2003;115:243–51. https://doi.org/10.1016/S0378-7753(03)00023-5.
[25] Frensch SH, Serre G, Fouda-Onana F, Jensen HC, Christensen ML, Araya SS, et al. Impact of iron and hydrogen peroxide on membrane degradation for polymer electrolyte membrane water electrolysis: Computational and experimental investigation on fluoride emission. Journal of Power Sources 2019;420:54–62. https://doi.org/10.1016/j.jpowsour.2019.02.076.
[26] Jahnke T, Futter G, Latz A, Malkow T, Papakonstantinou G, Tsotridis G, et al. Performance and degradation of Proton Exchange Membrane Fuel Cells: State of the art in modeling from atomistic to system scale. Journal of Power Sources 2016;304:207–33. https://doi.org/10.1016/j.jpowsour.2015.11.041.
[27] Chandesris M, Vincent R, Guetaz L, Roch J-S, Thoby D, Quinaud M. Membrane degradation in PEM fuel cells: From experimental results to semi-empirical degradation laws. International Journal of Hydrogen Energy 2017;42:8139–49. https://doi.org/10.1016/j.ijhydene.2017.02.116.
[28] Ferreira RB, Falcão DS, Pinto AMFR. Simulation of membrane chemical degradation in a proton exchange membrane fuel cell by computational fluid dynamics. International Journal of Hydrogen Energy 2021;46:1106–20. https://doi.org/10.1016/j.ijhydene.2020.09.179.
[29] Pozio A, Silva RF, De Francesco M, Giorgi L. Nafion degradation in PEFCs from end plate iron contamination. Electrochimica Acta 2003;48:1543–9. https://doi.org/10.1016/S0013-4686(03)00026-4.
[30] Robin C, Gerard M, d'Arbigny J, Schott P, Jabbour L, Bultel Y. Development and experimental validation of a PEM fuel cell 2D-model to study heterogeneities effects along large-area cell surface. International Journal of Hydrogen Energy 2015;40:10211–30. https://doi.org/10.1016/j.ijhydene.2015.05.178.
[31] Oxygen starvation analysis during air feeding faults in PEMFC | Elsevier Enhanced Reader n.d. https://doi.org/10.1016/j.ijhydene.2010.08.028.
[32] da Fonseca R, Bideaux E, Gerard M, Jeanneret B, Desbois-Renaudin M, Sari A. Control of PEMFC system air group using differential flatness approach: Validation by a dynamic fuel cell system model. Applied Energy 2014;113:219–29. https://doi.org/10.1016/j.apenergy.2013.07.043.
[33] Schott P, Baurens P. Fuel cell operation characterization using simulation. Journal of Power Sources 2006;156:85–91. https://doi.org/10.1016/j.jpowsour.2005.08.034.
[34] Wang Y, Northwood DO. Effects of O2 and H2 on the corrosion of SS316L metallic bipolar plate materials in simulated anode and cathode environments of PEM fuel cells. Electrochimica Acta 2007;52:6793–8. https://doi.org/10.1016/j.electacta.2007.05.001.
[35] Sridhar N, Cragnolino GA. Applicability of Repassivation Potential for Long-Term Prediction of Localized Corrosion of Alloy 825 and Type 316L Stainless Steel. CORROSION 1993;49:885–94. https://doi.org/10.5006/1.3316014.
[36] Ruvinskiy PS, Bonnefont A, Pham-Huu C, Savinova ER. Using Ordered Carbon Nanomaterials for Shedding Light on the Mechanism of the Cathodic Oxygen Reduction Reaction. Langmuir 2011;27:9018–27. https://doi.org/10.1021/la2006343.
[37] Chandesris M, Médeau V, Guillet N, Chelghoum S, Thoby D, Fouda-Onana F. Numerical modelling of membrane degradation in PEM water electrolyzer: Influence of the temperature and current density 2015:8.
[38] Sethuraman VA, Weidner JW, Haug AT, Motupally S, Protsailo LV. Hydrogen Peroxide Formation Rates in a PEMFC Anode and Cathode: Effect of Humidity and Temperature. J Electrochem Soc 2007;155:B50. https://doi.org/10.1149/1.2801980.
[39] Sedighi M, Rostami AA. Electrodeposition of Pt/CeO2/MWCNT as Hydrogen Peroxide Scavenger for Chemical Degradation Mitigation of Nafion Membrane. J Electrochem Soc 2019;166:D435. https://doi.org/10.1149/2.0901910jes.
[40] Wang F, Tang H, Pan M, Li D. Ex situ investigation of the proton exchange membrane chemical decomposition. International Journal of Hydrogen Energy 2008;33:2283–8. https://doi.org/10.1016/j.ijhydene.2008.01.052.
[41] Mu S, Xu C, Gao Y, Tang H, Pan M. Accelerated durability tests of catalyst layers with various pore volume for catalyst coated membranes applied in PEM fuel cells. International Journal of Hydrogen Energy 2010;35:2872–6. https://doi.org/10.1016/j.ijhydene.2009.05.022.
[42] Liu H, Coms FD, Zhang J, Gasteiger HA, LaConti AB. Chemical Degradation: Correlations Between Electrolyzer and Fuel Cell Findings. In: Büchi FN, Inaba M, Schmidt TJ, editors. Polymer Electrolyte Fuel Cell Durability, New York, NY: Springer New York; 2009, p. 71–118. https://doi.org/10.1007/978-0-387-85536-3_5.
[43] Zhu F, Luo L, Wu A, Wang C, Cheng X, Shen S, et al. Improving the High-Current-Density Performance of PEMFC through Much Enhanced Utilization of Platinum Electrocatalysts on Carbon. ACS Applied Materials & Interfaces 2020. https://doi.org/10.1021/acsami.0c06981.
[44] Curtin D, Lousenberg R, Henry T, Tangeman P, Tisack M. Advanced materials for improved PEMFC performance and life. Journal of Power Sources 2004;131:41–8. https://doi.org/10.1016/j.jpowsour.2004.01.023.
[45] Kawai K, Mabuchi T, Tokumasu T. Molecular Dynamics Analysis of Proton Diffusivity in Hydrated Nafion Membranes Contaminated with Ferrous Ions. Macromol Theory Simul 2020;29:1900047. https://doi.org/10.1002/mats.201900047.
[46] Kim DS, Welch C, Hjelm RP, Kim YS, Guiver MD. 10.36 - Polymers in Membrane Electrode Assemblies. In: Matyjaszewski K, Möller M, editors. Polymer Science: A Comprehensive Reference, Amsterdam: Elsevier; 2012, p. 691–720. https://doi.org/10.1016/B978-0-444-53349-4.00287-9.
[47] T. Jahnke, G. Futter , A. Latz, T. Malkow , G. Papakonstantinou, G. Tsotridis , P. Schott, M. Gerard, M. Quinaud, M. Quiroga, A.A. Franco, K. Malek h, F. Calle-Vallejo, R. Ferreira de Morais, T. Kerber, P. Sautet, D. Loffreda, S. Strahl, M. Serra, P. Polverino, C. Pianese, M. Mayur, W.G. Bessler et C. Kompis,. Performance and degradation of Proton Exchange Membrane Fuel Cells: State of the art in modeling from atomistic to system scale. Journal of Power Sources 2016;304:207–33. https://doi.org/10.1016/j.jpowsour.2015.11.041.
[48] Kreitmeier S. Factors determining the gas crossover through pinholes in polymer electrolyte fuel cell membranes. Electrochimica Acta 2012:8.
[49] Gebel G, Diat O. Neutron and X-ray Scattering: Suitable Tools for Studying Ionomer Membranes. Fuel Cells 2005;5:261–76. https://doi.org/10.1002/fuce.200400080.
[50] Gubler L, Dockheer SM, Koppenol WH. Radical (HO•, H• and HOO•) Formation and Ionomer Degradation in Polymer Electrolyte Fuel Cells. J Electrochem Soc 2011;158:B755. https://doi.org/10.1149/1.3581040.

[51] Futter GA. Physical modeling of chemical membrane degradation in polymer electrolyte membrane fuel cells: Influence of pressure, relative humidity and cell voltage n.d.
[52] Frensch SH. Impact of iron and hydrogen peroxide on membrane degradation for polymer electrolyte membrane water electrolysis_ Computational and experimental investigation on fluoride emission. Journal of Power Sources 2019:9.
[53] Frensch SHF Guillaume Serre , Frédéric Fouda-Onana , Henriette Casper Jensen , Morten Lykkegaard Christensen , Samuel Simon Araya , Søren Knudsen Kær. Impact of iron and hydrogen peroxide on membrane degradation for polymer electrolyte membrane water electrolysis: Computational and experimental investigation on fluoride emission. Journal of Power Sources 2019;420:54–62. https://doi.org/10.1016/j.jpowsour.2019.02.076.
[54] Wang X, Zhang L, Li G, Zhang G, Shao Z-G, Yi B. The influence of Ferric ion contamination on the solid polymer electrolyte water electrolysis performance. Electrochimica Acta 2015;158:253–7. https://doi.org/10.1016/j.electacta.2015.01.140.
[55] Tsotridis G, Pilenga A, De Marco G, Malkow T, European Commission, Joint Research Centre. EU harmonised test protocols for PEMFC MEA testing in single cell configuration for automotive applications. Luxembourg: Publications Office; 2015.
[56] Amphlett JC, Baumert RM, Mann RF, Peppley BA, Roberge PR, Harris TJ. Performance Modeling of the Ballard Mark IV Solid Polymer Electrolyte Fuel Cell: I . Mechanistic Model Development. J Electrochem Soc 1995;142:1–8. https://doi.org/10.1149/1.2043866.
[57] Ne B, Ha E, L K, B M. Bond graph modeling approach development for fuel cell PEMFC systems. Int J Hydrog Energy 2014;39:15224–31.
[58] Chu K, Ryu J, Sunwoo M. A lumped parameter model of the polymer electrolyte fuel cell 2007. https://doi.org/10.1016/J.JPOWSOUR.2007.05.108.
[59] Couenne F, Jallut C, Maschke B, Tayakout-fayolle M, Breedveld P. Structured modeling for processes: A thermodynamic network theory. Computers & Chemical Engineering 2008;32:1120–34. https://doi.org/10.1016/j.compchemeng.2007.04.012.
[60] Kebdani M. Modélisation dynamique basée sur l'approche bond graph d'une boucle fluide diphasique à pompage mécanique avec validation expérimentale n.d.:265.
[61] Rabih S, Turpin C, Astier S. Bond graph model of a PEM fuel cell stack. REPQJ 2008;1:329–34. https://doi.org/10.24084/repqj06.291.